Molecular Engineering of Fluoroether Electrolytes for Lithium Metal Batteries[†]

Yuxi Chen,[a] Elizabeth M.Y. Lee,[a] Phwey S. Gil,[a] Peiyuan Ma,[a] Chibueze V. Amanchukwu,[*a] and Juan J. de Pablo[*a‡]

Fluoroether solvents are promising electrolyte candidates for high-energy-density lithium metal batteries, where high ionic conductivity and oxidative stability are important metrics for design of new systems. Recent experiments have shown that these performance metrics, particularly stability, can be tuned by changing the fraction of ether and fluorine content. However, little is known about how different molecular architectures influence the underlying ion transport mechanisms and conductivity. Here, we use all-atom molecular dynamics simulations to elucidate the ion transport and solvation characteristics of fluoroether chains of varying length, and having different ether segment and fluorine terminal group contents. The design rules that emerge from this effort are that solvent size determines lithium-ion transport kinetics, solvation structure, and solvation energy. In particular, the mechanism for lithium-ion transport is found to shift from ion hopping between solvation sites located in different fluoroether chains in short-chain solvents, to ion-solvent co-diffusion in long-chain solvents, indicating that an optimum exists for molecules of intermediate length, where hopping is possible but solvent diffusion is fast. Consistent with these findings, our experimental measurements reveal a non-monotonic behavior of the effects of solvent size on lithium-ion conductivity, with a maximum occurring for medium-length solvent chains. A key design principle for achieving high ionic conductivity is that a trade-off is required between relying on shorter fluoroether chains having high self-diffusivity, and relying on longer chains that increase the stability of local solvation shells.

*

1 Design, System, Application

Lithium-ion batteries have a wide range of applications, from transportation to portable electronics. Replacing the anode with lithium metal increases the energy capacity of battery cells, but progress has been hindered by poor stability and extensive dendrite growth. Fluoroether solvent electrolytes offer promise for improving stability against the lithium metal anode and, in this work, we investigate how the molecular architecture and the size of the electrolyte solvent molecules impact the ion transport and local solvation environment of lithium (Li)-ions. Notably, we demonstrate that ionic conductivity can be controlled by the molecular structure of fluoroether electrolytes. A critical balance between high solvent self-diffusivity in short-chain solvents and low solvation free energy in long-chain solvents leads to an optimal solvent size for achieving high ionic conductivity, in agreement with experiments. This trade-off between solvent self-diffusivity and solvation free energy is shown to be an important criterion for design of fluoroether electrolytes with high lithium-ion conductivity and, more generally, it helps provide a comprehensive framework to guide selection of electrolytes for energy storage.

2 Introduction

Rechargeable lithium (Li)-ion batteries are a leading form of energy storage with applications ranging from transportation to portable electronics.[1,2] State-of-the-art lithium-ion batteries have limited energy density and capacity, owing to their graphite anodes.[3–5] Using lithium metal as the anode enhances the specific capacity of the battery cells because the metal has a high theoretical specific capacity (3,860 mAh/g) and a low negative electrochemical potential (–3.04 V versus standard hydrogen electrode).[4–7] However, extensive dendrite growth at the surface of lithium metal anodes raises safety concerns, and has precluded widespread adoption of lithium metal battery technology.[4,7] Dendrite growth poses significant challenges for development of lithium metal batteries that use conventional electrolytes, such as carbonates or ethers.[4,8]

Numerous efforts have been made to build safe, high-energy-density lithium metal batteries by engineering electrolytes characterized by high electrochemical stability and high ionic conductivity. For example, super-concentrated electrolytes are shown to increase the electrochemical stability of the battery cell, preventing dendrite growth when the electrolyte is in contact with the lithium metal anode. However, high salt concentration also increases the viscosity of the electrolytes, lowering the ion conductivity.[9,10] Other studies have used electrolytes based on nitriles[11] and sulfones[12,13] to improve ionic conductivity and electrolyte safety but these materials also suffer from low stability against lithium metal anodes. Fluorinated compounds can suppress the dendrite growth at the surface of the lithium metal anode[14]. Several studies have shown that fluorinated electrolytes react with

the lithium anode and form a protective solid electrolyte interphase (SEI) layer composed of lithium fluoride, thereby preventing the anode from further degradation.[14–16] For example, some ether-based electrolytes are reported to have improved stability and reduced anode degradation when fluoroethylene carbonates are used as additives.[17] Despite these recent successes based on addition of fluorinated compounds to ether-based solvents to suppress dendrite growth, ether-based solvents themselves still remain unstable and susceptible to decomposition, raising the need for alternative electrolytes based on fluorinated compounds.

To address this challenge, several groups have proposed fluoroether electrolyte solvents formed by covalently bound fluorinated groups to ether chains.[18,19] Fluoroether electrolytes with ether moieties sandwiched by fluorinated terminal groups exhibit ionic conductivities as high as 1.3 mS/cm at 25 °C, and oxidative stabilities as high as 5.2V_{Li}[20]. Similarly, fluoroether electrolyte solvents with fluorinated groups at the ends of each ether solvent chain exhibit higher conductivity than inverted designs, i.e., fluorinated groups sandwiched by ether terminal units.[20,21] Despite the apparent chemical tunability of these electrolytes, the effect of fluoroether solvent structures on the underlying ion transport mechanism remains unclear. It is experimentally challenging to directly probe ion solvation structures and quantify their inherent stability[22]. Understanding such structures, however, is critical for design of this class of electrolyte solvents from the constituent atomic building blocks and molecular architectures.

Atomistic models and computer simulations, such as classical molecular dynamics (MD), are ideal tools for relating molecular-level structures to macroscopic transport and stability measurements for battery electrolytes. The time and length scales accessible to MD simulations match well with those associated with ion transport.[23] For instance, MD simulations have been readily used to study solvation structures and ionic transport in ionic liquids[24,25], polymer electrolytes[26–28], and polyelectrolytes[23,29,30].

Herein, we employ all-atom MD simulations on six different fluoroether electrolyte solvent systems to understand how tuning molecular design parameters—such as the length of the ether segments in fluoroether chains and the number of fluorinated terminal groups in each chain—impact ion transport in the systems. We show that the diffusion mechanism of lithium (Li) ions strongly depends on the length of the fluoroether solvent chains, owing to changes in their ion-solvent coordination environment. We demonstrate that the stability of the ion-solvent coordination structure and the solvent chain mobility are critical for optimizing electrolyte solvents that can achieve high Li-ion conductivity.

3 Results and discussion

3.1 Atomistic fluoroether solvent modeling and validation

We use all-atom MD simulations to model our fluoroether molecules studied in this work. As illustrated in Figure 1, fluoroether molecules contain ether moieties covalently bonded to fluorinated functional terminal groups. We vary the length of ether chains and the number of fluorinated terminal groups and investigate how these two factors can affect the transport be-

haviors and local solvation environment of Li-ions. Each solvent molecule is labeled as E(N)F(M), where N is the length of ether segments in the center of the solvent molecule, and M is the number of fluorinated terminal groups (Figure 1); for example, E3F1 is used to designate fluoroethers with an ether segment having three ether units connected to one perfluorocarbon, -CF3, on each end.

Fluorinated ether solvent molecules were modeled using the OPLS all-atom force field[31]. We carried out MD simulations for each solvent system at a salt concentration of 1 M lithium bis(fluorosulfonyl)imide (LiFSA) (see the Computational Methods section). To capture the electrostatic interaction strengths in the electrolytes, we applied a charge scaling method to our forcefields as done previously.[32,33] Both our study (see Fig. S.1) and other theoretical works on ion pairing[32,33] indicate that reducing partial charges of ionic species is necessary because non-polarizable force fields like OPLS tend to overestimate electrostatic energies. We scaled the partial charges of lithium and FSA ions by a factor of 0.8 based on studies by Damas et al.[34], which are also widely adopted in modeling ion pairs and ionic liquids[32,33,35]. All other forcefield parameters remained unchanged (see the discussion on charge rescaling in the Sec. S1 in the Supplementary Materials).

We show the results of our simulations in Figure 2a, where we compare the calculated densities of pure fluoroether solvents (i.e., having no Li and FSA ions) from MD simulations to the density measurements from our experiments at 300 K[20]. Across all solvents, differences between our simulations and experiments are under 1.6% (see also Table S.1 in the Supplementary Material.) In Figure 2b, we show the Li-ion diffusivity in 1 M LiFSA electrolyte systems at 300 K, calculated from simulations and compared with experiments[20]. The simulation and experimental data follow the same trends; a lower Li-ion diffusivity is observed for bulkier electrolyte solvents, and the difference in their values is under a factor of three, indicating reasonable agreement between simulations and experiments. These results serve to validate our choice of molecular force field, and the charge scaling factor of 0.8. With this validation at hand, in what follows we proceed to examine different fluoroether electrolyte systems.

3.2 Solvent Dynamics and Lithium-Ion Diffusion Mechanisms

In analogy to glassy materials, we use glass transition temperature (T_g) as a metric to quantify the segmental mobility of the fluoroether solvent chains, where a high T_g indicates a low solvent chain mobility.[27,36] We calculated the T_g of the pure solvents and 1M LiFSA compared with experimental measurements (see Figure 2c). Simulations overestimate the T_g by roughly 50 K, possibly due to the faster cooling rate used in our simulations than in experiments. For instance, T_g can increase by about 5 K when the cooling rate increases by a factor of ten.[37] Regardless, the simulation data qualitatively reproduces the same trend as experimental data, where not only T_g increases with increasing chain length, but also with the addition of salts (by about ∼ 4K). This increase in T_g upon addition of salts indicates that the coordina-
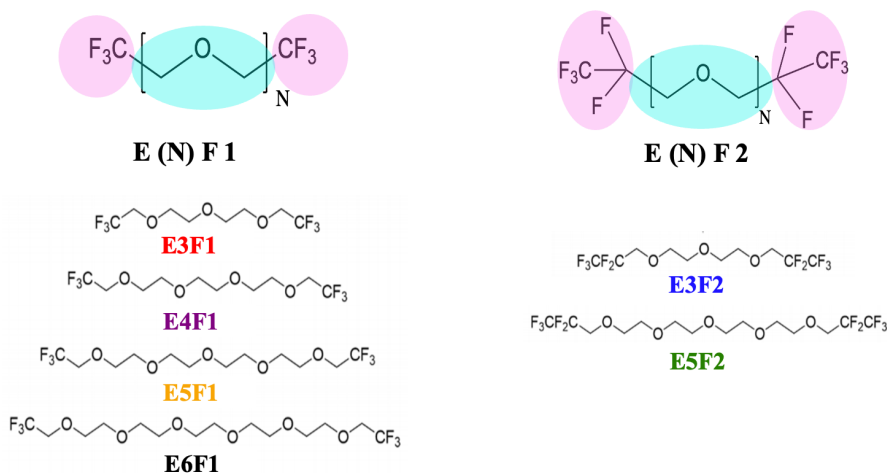
Fig. 1 Chemical structures of fluoroether electrolyte solvents studied in this work. Ether segments (in blue) are sandwiched between fluorinated terminal groups (in pink). For simplicity, each solvent is labeled as E(N)F(M), where (N) and (M) refer to the number of ether oxygens and fluorinated terminal groups, respectively.
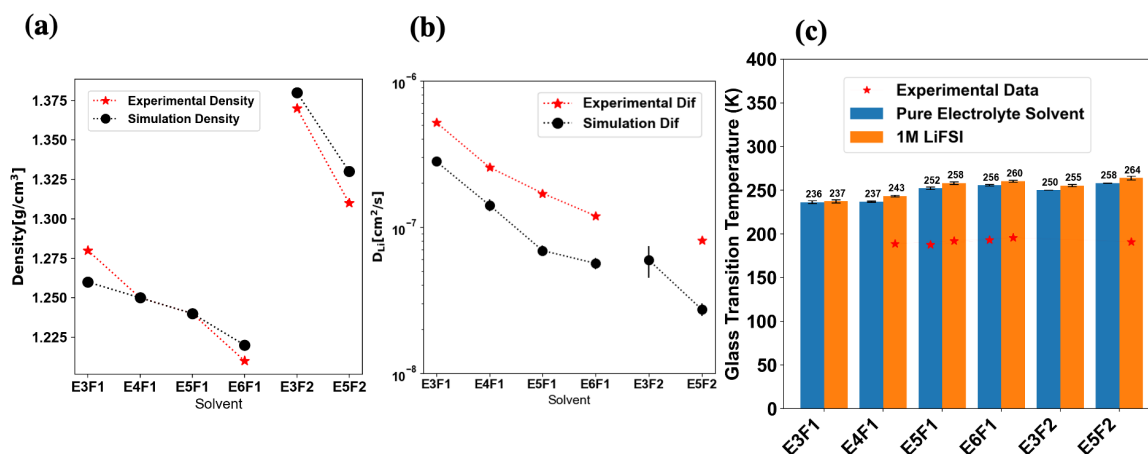

Fig. 2 Computational model validation by comparing simulation results with experiments on pure solvents and 1 M LiFSA systems. (a) Li-ion density from MD simulations (in black) at 300 K and measured Li-ion density from experiments (in red) at 300 K. (b) Li-ion diffusivity from MD simulations (in black) and experiments (in red) at 300 K. Experimental diffusivity data for E3F2 are not available, and are therefore omitted in the figure. (c) Glass transition temperatures of pure solvent systems and 1M LiFSA systems, calculated using MD simulations with a cooling rate of 14.2 K/ns. Each simulation data point is an average over three independent MD simulations with an error bar for the standard error. Red star markers indicate available experimental data.

tion between solvent molecules and Li-ions restricts the system's mobility and slows down solvent motion. Comparing the F2 family with the F1 family, T_g is higher for the F2 family due to their higher molecular weight. These results on solvent size-dependent trends in T_g indicate that slower mobility is associated with longer and heavier chains.

To investigate the diffusion mechanisms of Li-ions, we measured the Li-ion diffusivity (Figure 3a) and solvent molecule self-diffusivity (Figure 3b) for each of the 1M electrolyte systems from $T = 300$ to $425K$. The solvent self-diffusivity data indicate again that longer and heavier chains diffuse more slowly at all temperatures. Similarly, the Li-ion diffusivity decreases with increasing solvent size. These results suggest that ion and solvent diffusivities are strongly correlated via ion-solvent co-diffusion. To test this hypothesis, we re-plotted our diffusivity data by normalizing the temperature by the T_g of the pure solvents, thereby removing the effect of size-dependent solvent chain mobility from the Li-ion transport kinetics (see Figure 3c for Li-ion diffusivity and Figure 3d for solvent self-diffusivity in 1 M electrolyte system). Interestingly, Li-ion diffusivity data collapse into a single universal curve at high temperatures regardless of the chain length and the number of fluorinated terminal groups. The universal curve underscores that Li-ion diffusion is determined by the mobility of solvent molecules, i.e., the co-diffusion of Li-ions and solvent chains. We also calculated the anion diffusivities over a range of temperatures. (See Figure S.2 in the Supplementary Material.) The anions exhibit a behavior that is similar to that of the Li ions at high temperatures: the data collapse into a single universal curve after normalization by the glass transition temperature. Using the diffusivity data, we further estimated the lithium transference number. We used the same definition of the lithium transference number as in the experiments, $t_+ = D_{Li^+}/(D_{Li^+} + D_{FSA^-})$[20]. The results are shown in the Supplementary Information Figure S.2. The calculated transference numbers are consistent with experimental results.[20]

The solvent diffusivity in the 1M electrolyte systems are also included in Figure 3d over a range of temperatures, normalized by T_g. Instead of collapsing into a universal line as in Figure 3c, the data separate into two distinct regimes: one for shorter chain lengths (E3F1 and E3F2) and the other for longer chain lengths (more than 3 ether units). When Li-ions are co-diffusing with the solvent, the solvent diffusivity represents the mobility of the whole solvation shell (i.e., solvated Li-ions and the solvent). Although co-diffusion of Li-ions and solvents appear to be the dominant Li-ion transport mechanism (based on data from Figure 3c), the existence of two distinct regimes (as seen in Figure 3d) indicates that the propensity for the co-diffusion may depend on the solvent size.

3.3 Solvent-size Dependent Ion Speciation and Solvation Environment

Ion speciation is critical to battery performance, and the extent of Li-ion coordination with anions and/or solvent molecules impacts ionic conductivity.[8,38,39] We characterized the Li-ion local solvation environment in all systems considered here. Based on the coordination structure of the first solvation shell of Li-ion, we defined and classified all possible binding conformations of Li-ions into three categories.[23,40,41]: (1) *lithium-ion aggregates (LAG)*, where Li-ions and anions form aggregates, and are defined in our analysis to be those that do not interact with the solvents within the first solvation shell, (2) *contact ion pairs (CIP)*, where Li-ions interact with both solvents and anions, and (3) *solvent-separated ion pairs (SSIP)*, where Li-ions only coordinate with solvent molecules and not with anions (see Figure 4a for graphical illustrations).

The fraction of each ion speciation state in the fluoroether electrolytes at 1M salt and 300 K are plotted in Figure 4b. In the F1 family, populations of SSIP and CIP increase as the chain length increases. Notably, in the F1 family, only E3F1 has a significant population of LAG that represents unsolvated Li-ions, and a low population of CIP and SSIP compared to other solvents in the F1 family. Likewise, in the F2 family, the population of LAG is higher in shorter chains than in longer chains. When Li-ions form LAG with counter ions, they tend to aggregate in large clusters that are relatively immobile. Comparing the F1 with the F2 family solvents with the same number of ether units, we find that the F2 family solvents have a significantly larger population of LAG than the F1 family solvents, revealing a much better solvation environment for Li-ion in the F1 than in the F2 family solvents. These results suggest that the shorter ether chains and the additional fluorinated terminal groups prevent Li-ions from stably binding with the solvent molecules. To corroborate the ion speciation analysis, we calculated radial distribution functions (RDF) between Li-ions and the solvent molecules (Figure S.3 in the Supplementary Material). Based on the RDF results, Li-ion coordinates more readily with the oxygen atoms than with the fluorine atoms. Furthermore, Li-ions coordinate primarily with oxygens at the center of the ether segments than with terminal oxygens closest to the fluorinated terminal groups (see the RDF data in Figure S.4 in the Supplementary Material). This finding indicates that the bulky fluorinated terminal groups block Li-ions from coordinating with the oxygen atoms, and the electron withdrawing nature of fluorine may also have an effect. Although the fluorinated terminal groups do not interact with the Li-ions, they improve the oxidative stability of the solvents and effectively shield the ether groups, consequently suppressing dendrite growth.[17] At the same time, the ether segments interact with the Li-ions by solvating the ions, increasing the overall conductivity. To identify the most frequently occurring structural motifs for lithium ions, we calculated the binding motif frequencies between Li-ions and the solvent (Figure 5a) and between Li-ions and the anions (Figure 5b). Binding motifs are categorized based on the number of oxygen atoms in either the solvent molecule or the anion species in the first solvation shell of a Li-ion (see the descriptions in the Figure 5 caption). As seen in Figure 5a, the most frequent Li-ion-solvent binding motif for longer chains (E4F1 to E6F1) is to have two solvents, with a total number of six ether oxygens coordinating with each Li-ion, with no anions. These motifs yield six ether oxygens in the first solvation shell of the Li-ion, consistent with previous findings that each Li-ion needs five to six oxygens in the first solvation shell.[26,28] It is also worth noting that when
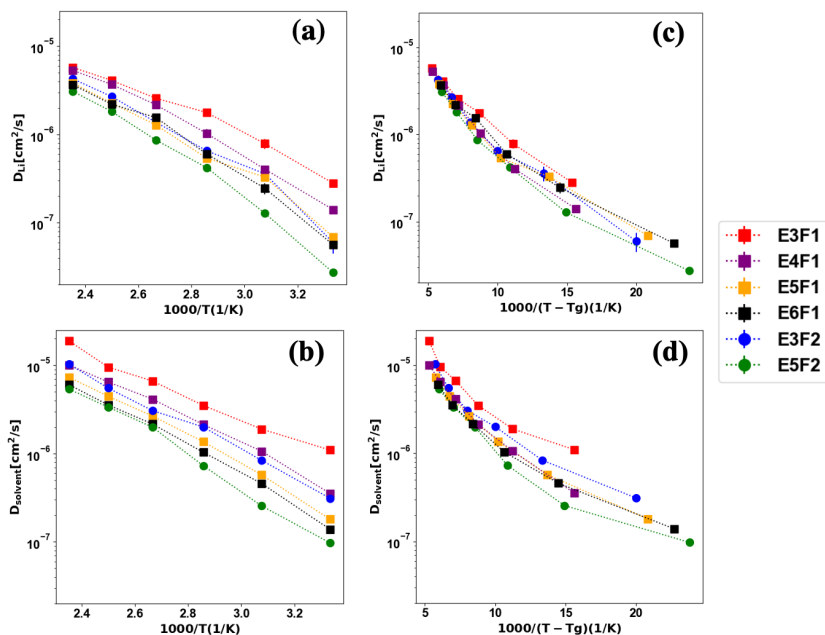
Fig. 3 Temperature dependence of Li-ion and solvent diffusion. (a) Li-ion diffusivity (D_{Li}) in 1M LiFSA plotted against the scaled inverse temperature, $1000/T$, where T is the absolute temperature. (b) Solvent self-diffusivity ($D_{solvent}$) in 1M LiFSA plotted against the scaled inverse temperature. (c-d) Same data as in (a-b) plotted against scaled reduced temperatures, $1000/(T - T_g)$, where T_g is the glass transition temperature of the pure solvents. Each data point represents an average over three independent MD simulations, with an error bar that corresponds to the standard deviation.

Li-ion is coordinated with more than one solvent chain, it can potentially serve as a "transient" cross-link between those solvent chains, and further slow down solvent motion.[42,43] This can also explain the much lower solvent diffusivities for longer chains observed in Figure 3d. When comparing F1 and F2 family solvents, we find a higher degree of coordination of anions by E5F2 than by E5F1 solvents, suggesting that the extra fluorinated terminal group leads to less stable coordination environments.

In contrast, in short solvent chains (E3s), the most prevailing configuration is to have three ether oxygens solvate each Li-ion (Figure 5a), resulting in much weaker ion-solvent binding than in other solvents. Likewise, more diverse anion binding motifs are seen in short solvent chains (Figure 5b). The weaker binding between Li-ions and solvent molecules in E3F1 and E3F2 leads to a less stable coordination shell for Li-ions. Additionally, there is a large amount of LAG in the E3 family (see Figure 4), hindering ion-solvent co-diffusion because a greater number of Li-ions stay within immobile clusters with anions. This data also help rationalize the two distinct regimes of solvent diffusivity in Figure 3d: the presence of LAG in shorter chains but not in longer chains. Indeed, we also calculated the time-dependent correlation function between Li-ion and solvent displacements (see Figure S.5 in the Supplementary Material), and find that ion-hopping rates in the E3 family are faster than in other solvents. Therefore, in short solvent chains, Li-ions can readily bind and unbind from the solvent chains, leading to frequent Li-ion hopping between ion solvation sites in different solvent chains.

In Figure 5c, we show MD snapshots of the representative configurations of Li-ion binding motifs in large (E5F1) and small (E3F1 and E3F2) size solvents (see Figure S.6 in the Supplemen-

tary Material for the other solvent systems). The dominant configuration in E5F1 has a significantly larger frequency ($\sim 60\%$) than that in the E3 family ($\sim 30\%$). This indicates that in longer chains, the local coordination environment of Li-ions remains relatively constant over time, while in shorter chains, the local environment is constantly changing. Consequently, Li-ions tend to co-diffuse more with solvent molecules in longer chain solvents than in shorter chain solvents. In shorter chain systems, on the other hand, there is more ion hopping between different molecules.

3.4 Ion Solvation Free Energy

The thermodynamics of ion solvation, usually characterized by the free energy of ion solvation, plays a key role in determining the solvent-specific redox potential.[44,45] We carried out thermodynamic integration (TI) to calculate the solvation free energy, ΔG_{ion}^{sol}, of Li-ions in each solvent. Solvation free energy calculations started by tuning electrostatic and dispersion interactions via a two-step approach: we first turned off the Coulomb interaction between Li-ion and the rest of the system and then later turned off the van der Waals (vdw). (See the Computational Methods section; our methodology is also schematically described in Figure 6c.) The TI results are shown in Figure 6a. The solvation free energy is negative in all cases, indicating the ions prefer to be surrounded by solvent molecules than by vacuum. Additionally, the solvation free energy decreases with increasing chain length for both F1 and F2 family solvents. For instance, the difference in the solvation free energy between the shortest chain, E3F1, and the longest chain, E6F1, is $\sim 7k_BT$ or $\sim 18kJ/mol$. We know that the higher magnitude of solvation energy indicates stronger bind-
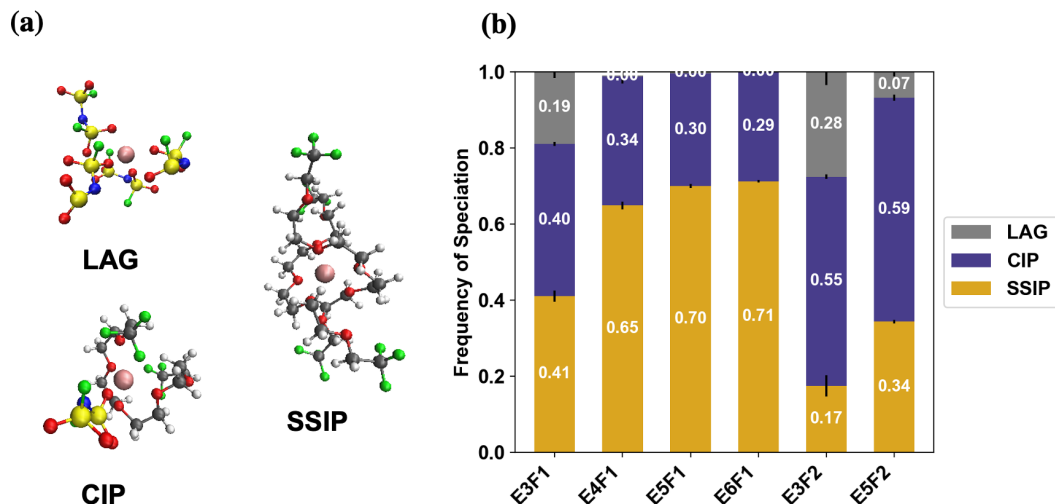
Fig. 4 Ion speciation trends at 300K. (a) Schematics of the three most common states of ion specification: Li-ion aggregates (LAG), contact ion pairs (CIP), and solvent separated ion pairs (SSIP). Li-ions are depicted in pink spheres; oxygens are in red; carbons are in dark gray; fluorines are in green. (b) The fraction of Li-ions in each speciation state across several fluoroether electrolytes. Frequencies are averaged over three independent MD simulations with error bars indicating standard deviations.
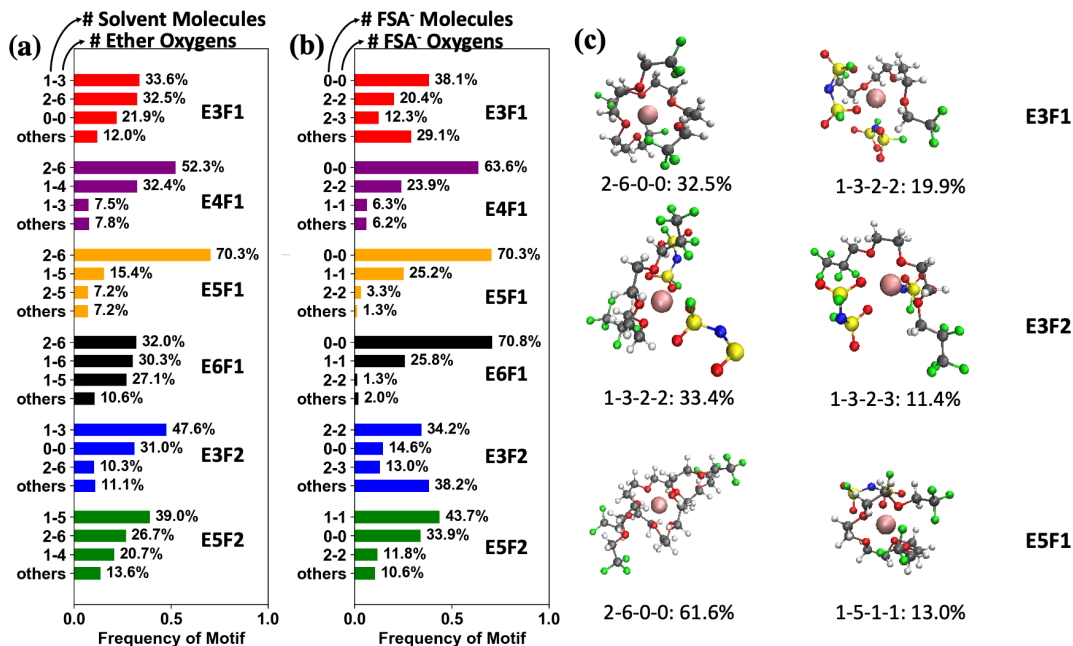

Fig. 5 Population of Li-ion binding motifs at 300K. (a) Frequency of Li-ion binding motifs between Li-ion and the solvent. The Li-ion-solvent binding motifs are labeled as A-B, where each letter refers to the number of solvent molecules (A) and the total number of ether oxygens (B) coordinating with a Li-ion within the first solvation shell. (b) Frequency of Li-ion binding motifs between Li-ion and anions. The Li-ion-anion binding motifs are labeled as C-D, where each letter refers to the number of anion molecules (C) and the total number of oxygens from the anions coordinating with a Li-ion within the first solvation shell. (c) Snapshots of the most frequent binding motifs of Li-ion in the selected solvent system (E3F1, E3F2, E5F1). The binding motifs are labeled with a combined 4-digit number, A-B-C-D, using the same definition for each letter. Li-ions are depicted in pink spheres; oxygens are in red; carbons are in dark gray; fluorines are in green.

ing between ions and solvent chains. These results confirm that longer solvent chains form more stable structures with Li-ion.

Since the primary source of electrostatic forces comes from the cation-anion interaction, we performed another set of TI calculations using the vdw forces alone, to isolate the energetic contribution of the Li-solvent interaction from the total free energy (see the Methods section). The resulting solvation free energy data from only the Li-solvent interaction is shown in Figure 6b. Within each F1 and F2 solvents, the vdw solvation free energy decreases with increasing ether segment length, as seen earlier in Figure 6a. However, when comparing between F1 and F2 solvents—i.e., solvents having the same number of ether units but a different number of fluorinated terminal groups –the F2 solvents both have a lower total solvation free energy but higher vdw solvation free energy than the F1 solvents. This result suggests that there is a higher fraction of cation-anion interaction in the F2 family than in the F1 family, supported by a larger fraction of LAG and more anions coordinating Li-ions in binding motifs found in the F2 family solvents compared to the F1 family (see Figures 4 and 5).

Interestingly, the magnitude of the solvation free energy (with or without electrostatic interactions) follows a similar trend as the measured oxidative stability in the F1 family[20], where both quantities increase with increasing solvent ether chain length. The higher the magnitude of the solvation free energy (i.e., more negative), the greater the stability of the solvation shell. It has been shown that when solvents form complexes with Li-ions (i.e., Li-ions are stabilized within the solvation shell), the oxidative stability increases.[46][47] Therefore, our results suggest that Li-ion solvation free energy may be a molecular fingerprint for measuring electrolyte oxidative stability.

Finally, we quantify the stability of various solvation structures via free energy calculations with enhanced sampling simulations. We used the Adaptive Biasing Force (ABF) algorithm[48] with MD to compute changes in the free energy with the coordination number between Li-ion and the ether oxygens from solvent molecules (see the Computational Methods section). Here, we defined the collective variable to be the coordination number exclusively between Li-ion and the ether oxygens from solvent molecules for the purpose of analyzing the binding between Li-ion and solvent molecules only. As seen in Figure 6d, free energies are referenced to their free energy minima, defined as the optimal number of ether units in the first solvation shell of each Li-ion to stabilize the ions. In each free energy profile, there is only one minimum, where the free energy rapidly increases by $\sim 10 k_B T$ or $\sim 25 kJ/mol$ with only small perturbations away from the minima. The optimal coordination number increases with an increasing number of ether units. Additionally, for solvent chains with the equal length of ether segments, those with a single fluorinated terminal group on each end have a higher coordination number than chains with two fluorinated terminal groups.

In Figure 6, we depict representative structures of solvents bound to Li-ions. In longer chains (E4-E6), individual Li-ions are tightly wrapped around by solvent chains, thereby hindering Li-ions from escaping away from the solvents. On the contrary, in the short chains (E3's), there are large openings in the solvation shell for Li-ions to interact with the anions and even unbind from the solvents. These observations strengthen our argument that longer solvent chains can better stabilize Li-ion than the shorter ones.

3.5 Optimizing Solvent for Lithium-Ion Conductivity

We calculated the ionic conductivity of each system at 300K by separating it into the individual contributions from uncorrelated ion motions, i.e. Li-ion self conductivity (σ_{Li}^s) and FSA-anion self conductivity (σ_{FSA}^s), and correlated ion motions, i.e. Li-ion distinct conductivity (σ_{Li}^d), FSA-anion distinct conductivity (σ_{FSA}^d), and cross conductivity between Li-ion and FSA-anion ($\sigma_{Li,FSA}^d$).[23,49–52]:

$$\sigma = \sigma_{Li}^s + \sigma_{FSA}^s + \sigma_{Li}^d + \sigma_{FSA}^d - 2 * \sigma_{Li,FSA}^d, \tag{1}$$

Readers are referred to the Computational Methods section for definitions and a description of the protocol for calculation of the various terms in Equation 1. In Figure 7a, we show a comparison between experimentally measured ionic conductivities and the results of our simulations. We can see that both sets of values follow the same trend: the highest ionic conductivity at 300 K is achieved at the intermediate chain length of four ether units (E4).We can now explain these data based on our MD simulations. In shorter chains (E3), both the weak binding between Li-ions and solvent molecules and the large population of LAG serve to lower the ionic conductivity. However, in longer chains, the primary transport mechanism is the co-diffusion of Li-ions and solvent molecules; thus, the ionic conductivity is lower in longer chain lengths (E5-E6).In Figure 7b we also show the contribution from each individual term in Equation 1. In shorter chains (E3), the high contribution from the cation-anion correlation term ($\sigma_{Li,FSA}^d$) greatly influences the total conductivity, which is consistent with our previous analysis. In longer chains, the low total conductivity mainly comes from the low self conductivity terms ($\sigma_{Li}^s, \sigma_{FSA}^s$), which arise from the low ionic diffusivity encountered in these systems. Therefore, achieving high ionic conductivity requires a trade-off between a solvent high self-diffusivity (which is favored with shorter chains) and the stability of the solvation shell (which is favored by longer chains). These insights could be useful for design of fluoroether solvents that optimize the total ionic conductivity, *i.e.*, useful design rules are to identify solvents with high self-diffusivity and better ionic coordination capabilities (a stable solvation shell for Li-ions).

4 Conclusion

The knowledge of lithium (Li)-ion transport mechanisms in battery electrolytes is fundamental to the design of electrolytes that enhance the battery cell's ionic conductivity. In this work, we used atomistic molecular dynamics (MD) simulations to study fluoroether electrolyte solvents, which have consecutive ether units sandwiched by fluorinated terminal groups. MD simulations predict that lithium ions are coordinated by ether segments, revealing that ether-segments in fluoroether electrolytes are responsible for the high ion conductivity measured in our recent experimental study[20]. Additionally, we find that the fluorinated terminal groups shield ether groups from directly contacting lithium an-
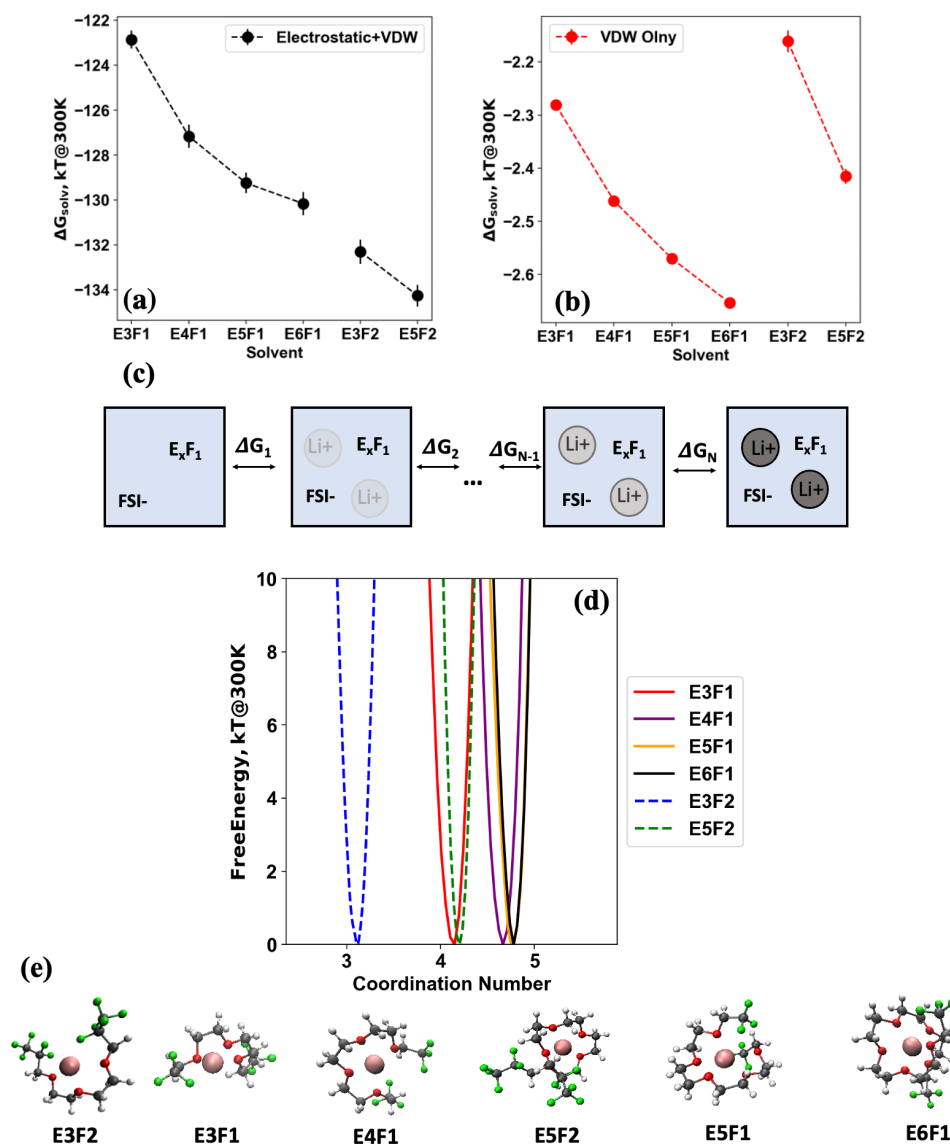
Fig. 6 Analysis of Li-ion solvation free energies (ΔG_{solv}) and their solvation shell structures. (a) Thermodynamic integration (TI) results showing the total solvation free energy—from both electrostatic and van der Waals (vdw) interactions—between Li-ions and the rest of the system (anions and the solvent). (b) TI results showing only the vdw interaction. Data in panels (a-b) are averaged over three independent MD simulations with error bars indicating standard deviations. (c) Schematic of solvation free energy calculations using TI. To calculate the total solvation free energy of Li-ion, we gradually turned on the coulombic and dispersion interactions between Li-ions and the rest of the system, and added the changes in the free energy between each images (ΔG_i). (d) Free energy profile of Li-ions in fluoroether solvents calculated using the adaptive biasing force method, where the collective variable is defined as the coordination number between Li-ions and the oxygen atoms in solvent molecules. All free energies are in the units of $k_B T$, where k_B is the Boltzmann constant, an T is the temperature, which is 300 K. (e) Ball-and-stick representations of lowest-energy conformations of Li-ions coordinated by solvent molecules.
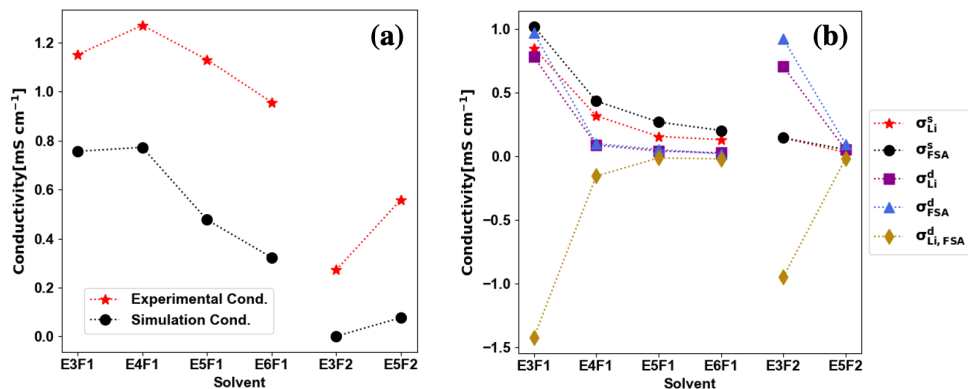
Fig. 7 Analysis of electrolyte ionic conductivity at 300K. (a) Ionic conductivity from MD simulations (in black) at 300 K and measured ionic conductivity from experiments (in red) at 300 K. (b) Contributions to total ionic conductivity from each individual term defined in Equation 1. Li-ion self conductivity plotted in red stars, FSA-anion self conductivity in black circles, Li-ion distinct conductivity in purple squares, FSA-anion distinct conductivity in blue triangles, cross cation-anion conductivity in gold diamonds.

ode, which is desirable for achieving high electrolyte stability.

We further investigated how the length of consecutive ether units and the number of fluorinated terminal groups affect the diffusion and local solvation environment of Li-ions. Based on our calculations of Li-ion diffusivity of fluoroether electrolytes over a range of temperatures, we find that the Li-ion diffusion mechanism depends on the length of the fluoroether solvent chains. In longer chains ($\sim$ 5 to 6 ether units), Li-ions tend to co-diffuse with the solvent chains, and ion hopping between solvation sites in different chains is rarely observed. In shorter chains ($\sim$ 3 ether units), we observe more frequent Li-ion hopping and less frequent ion-solvent co-diffusion. Additionally, large amounts of Li-ion aggregates exist in short chains because Li-ions are weakly bound to the solvent chains. Our free energy calculations show that larger solvent molecules with longer ether segments and a higher number of fluorinated terminal groups better stabilize Li-ion-solvent complexes than shorter molecules. Interestingly, both the absolute magnitude of the computed solvation free energy and the experimentally measured solvent oxidative stability increase with increasing solvent length, suggesting that the solvation free energy may provide a molecular signature of the strength of oxidative stability of these electrolytes.

Our simulations predict that intermediate-length fluoroether solvents ($\sim$ 4 to 5 ether units) with single fluorinated terminal groups have the highest ionic conductivity, in good agreement with our recent experiments. This finding reveals a trade-off between solvent chain mobility and local solvation shell stability for increasing ionic conductivity. In other words, larger solvent molecules with longer ether chains with a higher number of fluorinated terminal groups may compromise the overall diffusion

rate with slow solvent self-mobilities but in turn provide a more stable solvation shell for Li-ions. Therefore, there is an optimal solvent size for achieving the highest ionic conductivity. Both our simulations and experiments suggest that fluoroethers having $\sim$4 to 5 ether units with a single fluorinated terminal group on each solvent chain are the optimal solvents. Future studies will use these insights to screen fluoroether solvents with different architectural properties—such as branched fluoroethers[53] and fluoroethers with partially fluorinated terminal groups[21]—and investigate how their molecular structure influences ion transport. Combining such knowledge with machine learning models[54–56] may provide a promising tool for design of next-generation fluoroether electrolytes.

5 Computational Methods

Molecular dynamics (MD) simulations were performed using GROMACS version 2019 simulation packages.[57–59] Each simulation contained fluoroether solvent molecules, Li-ions, and FSA anions. Solvent molecules and Li-ions were parameterized using the OPLS-AA force field.[31,60] The fluoroalkly parameters were taken from E. Watkins et. al.[60] and all the other parameters were taken from W. Jorgensen et. al.[31]. All the partial charges were taken from the original OPLS-AA development and assigned based on atom types. FSA anions were parameterized using the CL&P force field.[61] We assigned partial charges of +0.8 to lithium cations and -0.8 to FSA anions. The simulation box, subjected to three-dimensional periodic boundary conditions, consisted of 300 to 400 solvent molecules with 1 M LiFSA in $5 \times 5 \times 5$ nm^3. See Table S.2 in Supplementary Material for details on the number of solvent molecules, Li-ions, and counterions in each simulation.

The simulation was started with a mixture of randomly placed ions and solvent molecules. The energy of this initial configuration was then minimized using the steepest decent minimization algorithm with a stopping criterion reached when the maximum total force of the system was less than 10.0 kJ/mol/nm. Electrolytes and ions were equilibrated for 10 ns in an NPT ensemble using a Berendsen barostat[58,59] at 1 bar, velocity-rescaling thermostat at 300 K, and a time step of 2 fs. The system was then further equilibrated using Parrinello-Rahman as the barostat and velocity-rescaling as the thermostat at the target temperature T and pressure of 1 bar.[62] Production runs were carried out in the NVT ensemble at the target temperature T using the Nose-Hoover thermostat for 300 ns.[63] MD trajectory data were stored every 10 ps. The particle-mesh-Ewald summation method was used to compute the electrostatic interactions.[64] Bond lengths between hydrogens and heavy atoms were constrained using the LINCS algorithm. A cutoff of 1.1 nm was set for both the Lennard-Jones (LJ) and Coulombic interactions.[65]

Glass transition temperatures of pure solvent and 1 M solution systems were calculated by cooling down the pure solvent and the 1 M solution systems, respectively, from 475 K to 50 K at a cooling rate of 14.2 K/ns. Then the specific volume was plotted against temperature, and first-order polynomials were used to fit the data. The glass transition temperature was found to be the temperature at which the two fitted lines intersect (See Figures S.7-S.8 in Supplementary Material for plots of specific volume versus temperature for representative electrolytes).

Diffusion coefficients, D, were calculated using the following equation,[66,67]

$$D = \frac{1}{6} \lim_{t \to \infty} \frac{d}{dt} \left(\sum_{i=1}^{N} [\vec{r}_i(t) - \vec{r}_i(0)]^2 \right), \tag{2}$$

where $\vec{r}_i(t)$ is the position vector of the ith atom at time t. To ensure that the probed dynamics entered the diffusive regime, we plotted $\log(\text{MSD})$ (where MSD stands for mean squared displacements) versus $\log(t)$ and measured D when the slope equaled one. See Figure S.9 in Supplementary Material for MSD plots of representative electrolytes. Error bars in diffusion coefficients were calculated by first breaking down a 300 ns-long trajectory into three independent segments and then averaging diffusion constants computed from each 100-ns segment.

Thermodynamic integration was carried out at 300K using the GROMACS software package. We employed the soft-core electrostatic potential and the Lennard-Jones (LJ) potential[68,69] to avoid the singularity effect caused by the divergence in $\langle \partial H / \partial \lambda \rangle$ with respect to λ in the following equation:[59,70–73]

$$G(p,T)^B - G(p,T)^A = \int_0^1 \left\langle \frac{\partial H}{\partial \lambda} \right\rangle_{NpT;\lambda} d\lambda, \tag{3}$$

where $G^B(p,T)$ is the Gibbs free energy at the end state (the solvated state) at constant pressure p and temperature T; $G^A(p,T)$ the Gibbs free energy at the beginning state (the unsolvated state) at constant pressure p and temperature T; and H the Hamiltonian; and λ the coupling parameter. To compute the solvation free energy, ΔG_{ion}^{sol}, we integrated the $\langle \partial H / \partial \lambda \rangle$ term with re-

spect to λ in Equation 3 using 20 λ windows, with each window carrying out 10 ns-long production runs in an NPT ensemble at $T =300$K and $p = 1$ atm. We adopted a two-step approach by first turning off the Coulombic interaction between Li-ions and the rest of the system in the first 10 windows and then turning off both the Coulombic and the van der Waals (vdw) interactions in the other 10 windows. To compute ΔG_{ion}^{sol} from the vdw interaction alone, we set the partial charges of the entire system to be zero and then gradually turned off the vdw interaction in the 20 λ windows.

Free energy profiles of Li-ions coordinated by solvent molecules were calculated using an enhanced sampling strategy based on the Adaptive Biasing Force (ABF) method[48] as implemented in the SSAGES software package[74] coupled to GROMACS. Enhanced sampling simulations were carried out in an NVT ensemble at 300K for 6 ns. The collective variable was the coordination number between Li-ions and the oxygen atoms in solvent molecules. The coordination number was calculated using a switching function,

$$s_{ij} = \frac{1 - \left(\frac{r_{ij} - d_0}{r_0} \right)^n}{1 - \left(\frac{r_{ij} - d_0}{r_0} \right)^m}, \tag{4}$$

where r_{ij} is the distance between particle i and particle j, r_0 is 0.05 nm, d_0 is 0.24 nm, n is 4, and m is 12.

The ionic conductivity of each system was calculated using the equation derived from the Green-Kubo equation, which relates the ionic conductivity with the microscopic charge current.[23,75,76]:

$$\sigma = \frac{1}{6k_BTV} \lim_{t \to \infty} \frac{d}{dt} \left\langle \sum_i \sum_j q_i q_j [\Delta \vec{r}_i \cdot \Delta \vec{r}_j] \right\rangle, \tag{5}$$

where $\Delta \vec{r}$ is defined as $\vec{r}(t) - \vec{r}(0)$, q_i and q_j represent charges of species i and species j. k_B is the Boltzmann's constant, T is the temperature (300K), and V is the volume. The total ionic conductivity can be further separated into contributions from correlated ion motions and uncorrelated ion motions, as described in Equation 1. Each term in Equation 1 is defined as:

$$\sigma_{Li}^s = \frac{1}{6k_BTV} \lim_{t \to \infty} \frac{d}{dt} \left\langle \sum_{i_{Li}} q_{i_{Li}}^2 [\Delta \vec{r}_{i_{Li}} \cdot \Delta \vec{r}_{i_{Li}}] \right\rangle, \tag{6}$$

$$\sigma_{FSA}^s = \frac{1}{6k_BTV} \lim_{t \to \infty} \frac{d}{dt} \left\langle \sum_{i_{FSA}} q_{i_{FSA}}^2 [\Delta \vec{r}_{i_{FSA}} \cdot \Delta \vec{r}_{i_{FSA}}] \right\rangle, \tag{7}$$

$$\sigma_{Li}^d = \frac{1}{6k_BTV} \lim_{t \to \infty} \frac{d}{dt} \left\langle \sum_{i_{Li}} \sum_{j_{Li} \neq i_{Li}} q_{i_{Li}} q_{j_{Li}} [\Delta \vec{r}_{i_{Li}} \cdot \Delta \vec{r}_{J_{Li}}] \right\rangle, \tag{8}$$

$$\sigma_{FSA}^d = \frac{1}{6k_BTV} \lim_{t \to \infty} \frac{d}{dt} \left\langle \sum_{i_{FSA}} \sum_{i_{FSA} \neq j_{FSA}} q_{i_{FSA}} q_{j_{FSA}} [\Delta \vec{r}_{i_{FSA}} \cdot \Delta \vec{r}_{j_{FSA}}] \right\rangle, \tag{9}$$

$$\sigma_{Li,FSA}^d = \frac{1}{6k_BTV} \lim_{t \to \infty} \frac{d}{dt} \left\langle \sum_{i_{Li}} \sum_{j_{FSA}} q_{i_{Li}} q_{j_{FSA}} [\Delta \vec{r}_{i_{Li}} \cdot \Delta \vec{r}_{j_{FSA}}] \right\rangle, \tag{10}$$

σ_{Li}^s is the Li-ion self conductivity, σ_{FSA}^s is the FSA anion self conductivity, σ_{Li}^d is the Li-ion distinct conductivity, σ_{FSA}^d is the FSA anion distinct conductivity, and $\sigma_{Li,FSA}^d$ is the distinct conductiv-

ity between Li-ion and FSA-anion. There is a significant amount of fluctuations in the distinct terms in Equation 1. Therefore, in order to get an accurate estimate of the derivatives in the distinct terms, we averaged over data from 10 independent 100 ns MD trajectories for each solvent system to calculate the collective MSD, from which we further calculated the derivatives.[77] It was ensured that the collective MSD has reached the linear regime in all cases.

6 acknowledgement

7 Supporting Information

The Supporting Information is available free of charge available at [URL].

Discussion of charge re-scaling effects; MD simulation details; comparison to experimental data; discussion of radial distribution functions; discussion of lithium-ion hopping studies; lithium-ion binding motifs; experimental data of ion conductivity; glass transition temperature calculations; lithium-ion mean square displacement plots in logarithmic scale (PDF)

Notes and references

1 J. M. Carrasco, L. G. Franquelo, J. T. Bialasiewicz, E. Galván, R. C. PortilloGuisado, M. M. Prats, J. I. León and N. Moreno-Alfonso, *IEEE Transactions on industrial electronics*, 2006, **53**, 1002–1016.

2 M. Beaudin, H. Zareipour, A. Schellenberglabe and W. Rosehart, *Energy for sustainable development*, 2010, **14**, 302–314.

3 J. B. Goodenough and K.-S. Park, *Journal of the American Chemical Society*, 2013, **135**, 1167–1176.

4 D. Lin, Y. Liu and Y. Cui, *Nature nanotechnology*, 2017, **12**, 194–206.

5 J.-M. Tarascon and M. Armand, *Materials for sustainable energy: a collection of peer-reviewed research and review articles from Nature Publishing Group*, World Scientific, 2011, pp. 171–179.

6 M. D. Tikekar, S. Choudhury, Z. Tu and L. A. Archer, *Nature Energy*, 2016, **1**, 1–7.

7 W. Xu, J. Wang, F. Ding, X. Chen, E. Nasybulin, Y. Zhang and J.-G. Zhang, *Energy & Environmental Science*, 2014, **7**, 513–537.

8 K. Xu, *Chemical reviews*, 2004, **104**, 4303–4418.

9 Y. Yamada and A. Yamada, *Journal of The Electrochemical Society*, 2015, **162**, A2406.

10 Y. Yamada, K. Furukawa, K. Sodeyama, K. Kikuchi, M. Yaegashi, Y. Tateyama and A. Yamada, *Journal of the American Chemical Society*, 2014, **136**, 5039–5046.

11 M. Kerner, D.-H. Lim, S. Jeschke, T. Rydholm, J.-H. Ahn and J. Scheers, *Journal of Power Sources*, 2016, **332**, 204–212.

12 C.-C. Su, M. He, P. C. Redfern, L. A. Curtiss, I. A. Shkrob and Z. Zhang, *Energy & Environmental Science*, 2017, **10**, 900–904.

13 B. Flamme, M. Haddad, P. Phansavath, V. Ratovelomanana-Vidal and A. Chagnes, *ChemElectroChem*, 2018, **5**, 2279–2287.

14 T. Li, X.-Q. Zhang, P. Shi and Q. Zhang, *Joule*, 2019, **3**, 2647–2661.

15 K. A. See, H.-L. Wu, K. C. Lau, M. Shin, L. Cheng, M. Balasubramanian, K. G. Gallagher, L. A. Curtiss and A. A. Gewirth, *ACS applied materials & interfaces*, 2016, **8**, 34360–34371.

16 S. Chen, J. Zheng, D. Mei, K. S. Han, M. H. Engelhard, W. Zhao, W. Xu, J. Liu and J.-G. Zhang, *Advanced materials*, 2018, **30**, 1706102.

17 Y. Lee, T. K. Lee, S. Kim, J. Lee, Y. Ahn, K. Kim, H. Ma, G. Park, S.-M. Lee, S. K. Kwak *et al.*, *Nano Energy*, 2020, **67**, 104309.

18 C. V. Amanchukwu, Z. Yu, X. Kong, J. Qin, Y. Cui and Z. Bao, *Journal of the American Chemical Society*, 2020, **142**, 7393–7403.

19 Z. Yu, H. Wang, X. Kong, W. Huang, Y. Tsao, D. G. Mackanic, K. Wang, X. Wang, W. Huang, S. Choudhury *et al.*, *Nature Energy*, 2020, **5**, 526–533.

20 P. Ma, P. Mirmira and C. V. Amanchukwu, *ACS Central Science*, 2021, **7**, 1232–1244.

21 Z. Yu, P. E. Rudnicki, Z. Zhang, Z. Huang, H. Celik, S. T. Oyakhire, Y. Chen, X. Kong, S. C. Kim, X. Xiao *et al.*, *Nature Energy*, 2022, 1–13.

22 Y. Marcus and G. Hefter, *Chemical reviews*, 2006, **106**, 4585–4621.

23 K. D. Fong, J. Self, K. M. Diederichsen, B. M. Wood, B. D. McCloskey and K. A. Persson, *ACS central science*, 2019, **5**, 1250–1260.

24 T. C. Lourenço, Y. Zhang, L. T. Costa and E. J. Maginn, *The Journal of Chemical Physics*, 2018, **148**, 193834.

25 P. Ray, A. Balducci and B. Kirchner, *The Journal of Physical Chemistry B*, 2018, **122**, 10535–10547.

26 M. A. Webb, B. M. Savoie, Z.-G. Wang and T. F. Miller III, *Macromolecules*, 2015, **48**, 7346–7358.

27 M. A. Webb, Y. Jung, D. M. Pesko, B. M. Savoie, U. Yamamoto, G. W. Coates, N. P. Balsara, Z.-G. Wang and T. F. Miller III, *ACS central science*, 2015, **1**, 198–205.

28 D. M. Pesko, M. A. Webb, Y. Jung, Q. Zheng, T. F. Miller III, G. W. Coates and N. P. Balsara, *Macromolecules*, 2016, **49**, 5244–5255.

29 B. Yu, A. M. Rumyantsev, N. E. Jackson, H. Liang, J. M. Ting, S. Meng, M. V. Tirrell and J. J. de Pablo, *Molecular Systems Design & Engineering*, 2021, **6**, 790–804.

30 J.-M. Y. Carrillo and A. V. Dobrynin, *Macromolecules*, 2011, **44**, 5798–5816.

31 W. L. Jorgensen, D. S. Maxwell and J. Tirado-Rives, *Journal of the American Chemical Society*, 1996, **118**, 11225–11236.

32 S. Mogurampelly and V. Ganesan, *The Journal of Chemical Physics*, 2017, **146**, 074902.

33 L. T. Costa, B. Sun, F. Jeschull and D. Brandell, *The Journal of chemical physics*, 2015, **143**, 024904.

34 G. B. Damas, A. B. Dias and L. T. Costa, *The Journal of Physical Chemistry B*, 2014, **118**, 9046–9064.

35 V. V. Chaban, I. V. Voroshylova and O. N. Kalugin, *Physical Chemistry Chemical Physics*, 2011, **13**, 7910–7920.

36 A. Killis, J.-F. LeNest, H. Cheradame and A. Gandini, *Die Makromolekulare Chemie*, 1982, **183**, 2835–2845.

37 P. G. Debenedetti and F. H. Stillinger, *Nature*, 2001, **410**, 259–267.

38 P. Johansson, *Physical Chemistry Chemical Physics*, 2007, **9**, 1493–1498.

39 A. France-Lanord and J. C. Grossman, *Physical review letters*, 2019, **122**, 136001.

40 G. S. Manning, *Accounts of Chemical Research*, 1979, **12**, 443–449.

41 G. S. Manning, *The journal of chemical Physics*, 1969, **51**, 924–933.

42 R. G. Linford, *Applications of electroactive polymers*, Springer, 1993, pp. 1–28.

43 H. Aydın, M. Şenel, H. Erdemi, A. Baykal, M. Tülü, A. Ata and A. Bozkurt, *Journal of Power Sources*, 2011, **196**, 1425–1432.

44 A. Baskin and D. Prendergast, *The Journal of Physical Chemistry Letters*, 2019, **10**, 4920–4928.

45 J. B. Straus and G. A. Voth, *The Journal of Physical Chemistry*, 1993, **97**, 7388–7391.

46 K. Yoshida, M. Nakamura, Y. Kazue, N. Tachikawa, S. Tsuzuki, S. Seki, K. Dokko and M. Watanabe, *Journal of the American Chemical Society*, 2011, **133**, 13121–13129.

47 X. Ren, P. Gao, L. Zou, S. Jiao, X. Cao, X. Zhang, H. Jia, M. H. Engelhard, B. E. Matthews, H. Wu *et al.*, *Proceedings of the National Academy of Sciences*, 2020, **117**, 28603–28613.

48 J. Comer, J. C. Gumbart, J. Hénin, T. Lelièvre, A. Pohorille and C. Chipot, *The Journal of Physical Chemistry B*, 2015, **119**, 1129–1151.

49 D. Dong and D. Bedrov, *The Journal of Physical Chemistry B*, 2018, **122**, 9994–10004.

50 D. Dong, F. Sälzer, B. Roling and D. Bedrov, *Physical Chemistry Chemical Physics*, 2018, **20**, 29174–29183.

51 J. G. McDaniel and C. Y. Son, *The Journal of Physical Chemistry B*, 2018, **122**, 7154–7169.

52 H. K. Kashyap, H. V. Annapureddy, F. O. Raineri and C. J. Margulis, *The Journal of Physical Chemistry B*, 2011, **115**, 13212–13221.

53 T. Zhou, Y. Zhao, M. El Kazzi, J. W. Choi and A. Coskun, *Angewandte Chemie International Edition*, 2022, e202115884.

54 R. Gómez-Bombarelli, J. N. Wei, D. Duvenaud, J. M. Hernández-Lobato, B. Sánchez-Lengeling, D. Sheberla, J. Aguilera-Iparraguirre, T. D. Hirzel, R. P. Adams and A. Aspuru-Guzik, *ACS central science*, 2018, **4**, 268–276.

55 E. M. Lee, T. Ludwig, B. Yu, A. R. Singh, F. Gygi, J. K. Nørskov and J. J. de Pablo, *The Journal of Physical Chemistry Letters*, 2021, **12**, 2954–2962.

56 N. E. Jackson, M. A. Webb and J. J. de Pablo, *Current Opinion in Chemical Engineering*, 2019, **23**, 106–114.

57 S. Páll, M. J. Abraham, C. Kutzner, B. Hess and E. Lindahl, International conference on exascale applications and software, 2014, pp. 3–27.

58 H. Bekker, H. Berendsen, E. Dijkstra, S. Achterop, R. Vondrumen, D. VANDERSPOEL, A. Sijbers, H. Keegstra and M. Renardus, 4th International Conference on Computational Physics (PC 92), 1993, pp. 252–256.

59 H. J. Berendsen, D. van der Spoel and R. van Drunen, *Computer physics communications*, 1995, **91**, 43–56.

60 E. K. Watkins and W. L. Jorgensen, *The Journal of Physical Chemistry A*, 2001, **105**, 4118–4125.

61 J. N. Canongia Lopes and A. A. Pádua, *Theoretical Chemistry Accounts*, 2012, **131**, 1–11.

62 G. Bussi, T. Zykova-Timan and M. Parrinello, *The Journal of chemical physics*, 2009, **130**, 074101.

63 D. J. Evans and B. L. Holian, *The Journal of chemical physics*, 1985, **83**, 4069–4074.

64 S. Páll and B. Hess, *Computer Physics Communications*, 2013, **184**, 2641–2650.

65 B. Hess, H. Bekker, H. J. Berendsen and J. G. Fraaije, *Journal of computational chemistry*, 1997, **18**, 1463–1472.

66 J. Habasaki and K. Ngai, *The Journal of chemical physics*, 2008, **129**, 194501.

67 M. S. Kelkar and E. J. Maginn, *The Journal of Physical Chemistry B*, 2007, **111**, 4867–4876.

68 T. C. Beutler, A. E. Mark, R. C. van Schaik, P. R. Gerber and W. F. Van Gunsteren, *Chemical physics letters*, 1994, **222**, 529–539.

69 M. R. Shirts and V. S. Pande, *The Journal of chemical physics*, 2005, **122**, 134508.

70 T. Steinbrecher, I. Joung and D. A. Case, *Journal of computational chemistry*, 2011, **32**, 3253–3263.

71 D. Van Der Spoel, E. Lindahl, B. Hess, G. Groenhof, A. E. Mark and H. J. Berendsen, *Journal of computational chemistry*, 2005, **26**, 1701–1718.

72 B. Hess, C. Kutzner, D. Van Der Spoel and E. Lindahl, *Journal of chemical theory and computation*, 2008, **4**, 435–447.

73 D. van der Spoel, E. Lindahl, B. Hess, C. Kutzner, A. van Buuren, E. Apol, P. Meulenhoff, D. Tieleman, A. Sijbers, K. Feenstra *et al.*, *Google Scholar There is no corresponding record for this reference*.

74 J. K. Whitmer, C.-c. Chiu, A. A. Joshi and J. J. De Pablo, *Physical review letters*, 2014, **113**, 190602.

75 D. Frenkel and B. Smit, *Understanding molecular simulation: from algorithms to applications*, Elsevier, 2001, vol. 1.

76 H. Liu and E. Maginn, *The Journal of chemical physics*, 2011, **135**, 124507.

77 P. Kubisiak and A. Eilmes, *The Journal of Physical Chemistry B*, 2020, **124**, 9680–9689.